Electronic Supplementary Material (ESI) for Materials Advances.

Supplementary material to the article Untangling the controversy on Ce^{3+} luminescence in $LaAlO_3$ crystals

Jan Pejchal, Vladimir Babin, Maksym Buryi, Valentyn Laguta, František Hájek, Juraj Páterek, Lenka Procházková-Prouzová, Lubomír Havlák, Vladimíra Czerneková, Vojtěch Vaněček, Václav Doležal, Jan Havlíček, Kateřina Rubešová, Petra Zemenová, Alexandra Falvey, Robert Král, Vladimir Pankratov, Kirill Chernenko

Table S1. LaAP crystals under investigation

Ce concentration (at%)	Growth atmosphere	note	Sample acronym
0	N_2	[1]	0-N2
0.5	N_2		0.5-N2
1	N_2	[1]	1-N2
20	N_2	[1]	20-N2
50	N_2	[1]	50-N2
100	N_2		100-N2
1	Ar+5%H_2	[1]	1-H2
20	Ar+5%H_2	[1]	20-H2
50	Ar+5%H_2	[1]	50-H2
100	Ar+5%H_2		100-H2
30	Ar+5%H_2	Balanced stoichiometry	30-H2-BS
0.001	Ar+5%H2	Balanced stoichiometry	0.001-H2-BS
0.003	Ar+5%H2	Balanced stoichiometry	0.003-H2-BS
0.01	Ar+5%H2	Balanced stoichiometry	0.01-H2-BS
0.1	Ar+5%H2	Balanced stoichiometry	0.1-H2-BS

1. La_2O_3 thermal analysis, mass spectroscopy and mass increase test

We performed simultaneous differential scanning calorimetry (DSC), thermogravimetric analysis (TG) and mass spectrometry (MS). It was found that the moisture and CO_2 that reacted with the La_2O_3 starting powder comprised about 5% of its mass, which means that the samples were non-negligibly La deficient.

The La_2O_3 powder was heated in a tube furnace under the N_2 atmosphere and temperature up to 1200 °C to remove the H_2O and CO_2 to eliminate the weighting errors.

Then the powder was kept in a glove box under a protective N_2 atmosphere (with concentration of residual O_2 and H_2O below 1 ppm) and weighted inside the glove box before each crystal growth procedure, which was performed as described in the article and in [1].

The thermal analysis of the La_2O_3 starting powder was performed with the simultaneous DSC–TG Setaram Themys 24 apparatus. All DSC–TG experiments were measured under the non-isothermal conditions with the heating rate of 10 K min^{-1} in the temperature range 25–1250 °C in alumina crucibles – one filled with sample and second one empty used as a reference, under the argon atmosphere (gas flow 20 ml min^{-1}, purity of 5N).

The DSC–TG apparatus was calibrated in the temperature range of 25–1300 °C using several standards (In, Sn, Zn, Al, Ag, and Au) and the accuracy of the TG was verified by $CuSO_4.5H_2O$ and $CaC_2O_4.xH_2O$. The standard deviation of the performed calibrations was in the range of ± 0.8 K. Processing of the obtained data was carried out by the Calisto Processing software. The mass spectrometry (MS) was performed using the quadrupole mass spectrometer Pfeiffer OmniStar GSD 320 equipped with a controlled and heated anti-corrosive quartz capillary, a coupling element enabling a connection with Themys 24, an yttria-coated iridium filament as a source of ionization, a secondary electron multiplier (SEM) as a detector (detection limit < 1 ppm of gases), and a turbo drag pumping system with an interstage turbo pump and a diaphragm pump as a vacuum source. The spectrometer enables a detection of the atomic masses in the range of 1-300 amu, however, only the selected masses of our interest were monitored in the MS measurements: related to H_2O (16, 17, and 18 amu); related to CH_x and CO_x (15, 29, and 12, 28, 44 amu, respectively); related to NH_3, N_2, and NO_x (17, 14, 28, 30, 46 amu). It is well known that the La_2O_3 powder has a tendency to absorb H_2O and CO_2 from the air to create hydroxides (lanthanum hydroxide $La(OH)_3$ or lanthanum oxy-hydroxide $LaO(OH)$) and partially carbonated lanthanum hydroxide ($La(OH)CO_3$) [2, 3]. This process of absorption was proved by the DSC-TG+MS measurements for our starting material as well, see figure S1. The first heating cycle in the range of 25-1250 °C revealed the strong effects between 267-395 °C and 423-537 °C. The first effect was ascribed to the decomposition of the lanthanum hydroxides and carbonated lanthanum hydroxide as reported in [2, 3]. The products of these processes were lanthanum oxy-hydroxide ($LaO(OH)$) and lanthanum oxy-carbonate ($La_2O_2CO_3$). The second effect is related to the decomposition of the $LaO(OH)$ into La_2O_3 by releasing H_2O. Finally, the $La_2O_2CO_3$ product decomposes above ca. 550 °C into pure La_2O_3 accompanied by escape of CO_2. All these processes are well documented by MS curves of H_2O and CO_2, see figure S1. The TG curve also proved that the thermal treatment of the La_2O_3 starting powder leads to the mass loss of ca. 4.5 %.

Based on these results the pre-heating procedure for the La_2O_3 starting material was established and further quality checked by control measurements, which justified the correctness of the pre-heating procedure. However, when the pre-heated material was kept in the glovebox with N_2 protective atmosphere ($H_2O<1$ ppm, $O_2<1$ ppm), the DSC-TG-MS experiment revealed weak effects related to the escape of H_2O and CO_2 from the powder, see figure S2. The total mass change was low, reaching ca. 0.3 mass%, however, still detectable. The origin of such a contamination (H_2O and CO_2) is so far unknown requiring further study, whether it is related to an inappropriate handling during the pre-heating process or an absorption from a storing container in the glovebox.

Nevertheless, the La_2O_3 powder is highly sensitive, when exposed to the air atmosphere, resulting in the sorption of H_2O and CO_2 and their reaction under the formation of the respective hydroxides and the mixed carbonates. In figure S3, the mass increase in ca. 100 min period when exposed to the air atmosphere (at room temperature and relative humidity rH ca. 25 %) is displayed. In such time, the La_2O_3 powder was able to absorb ca. 2 mass%. Such increase is comparable with highly hygroscopic halides e.g. $LaCl_3$, $EuBr_2$, etc., even though the reported values were measured at higher relative humidity rH 40%, see [4].

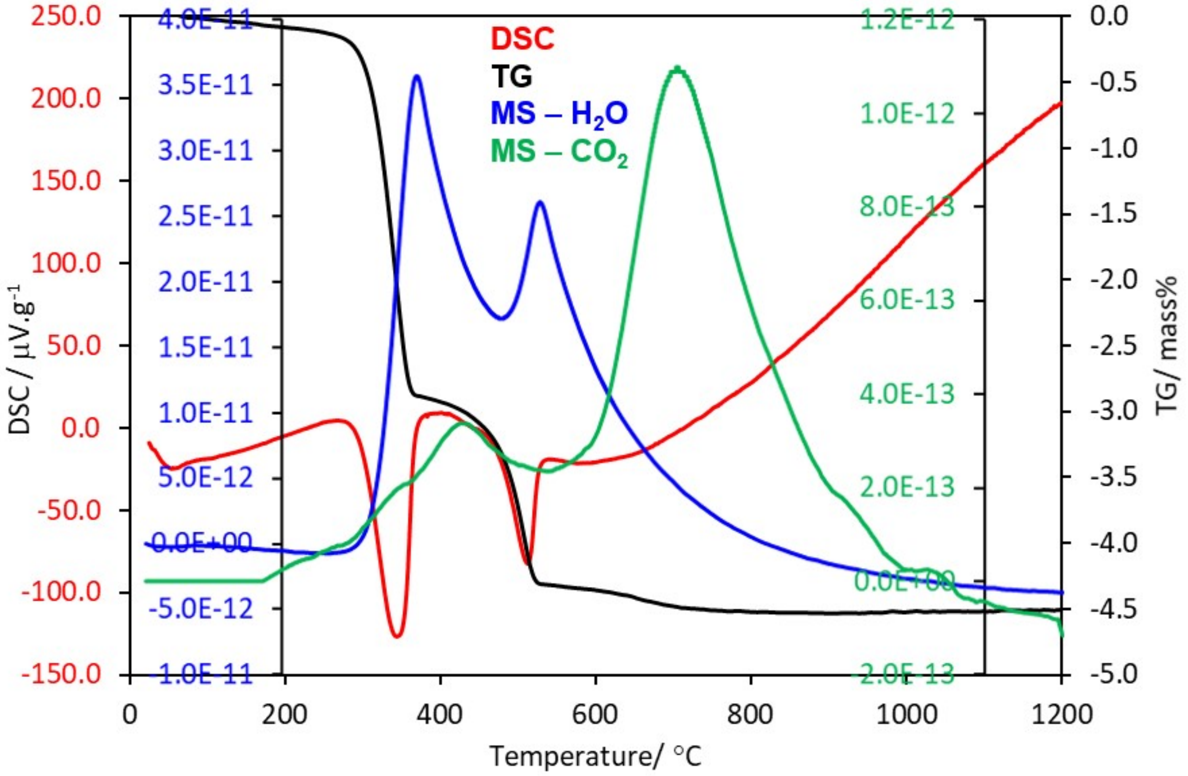

Figure S1. DSC-TG-MS curves of the La_2O_3 starting material.

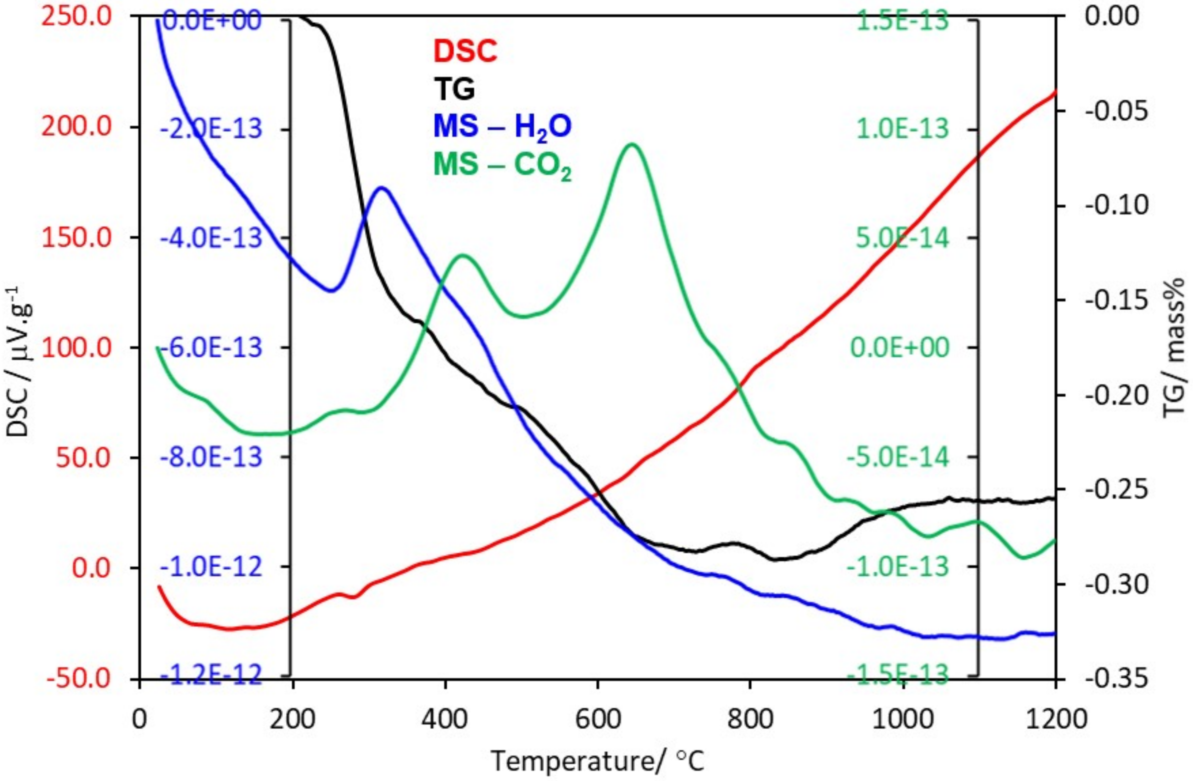

Figure S2. DSC-TG-MS curves of the La_2O_3 pre-heated powder after being kept in glovebox under N_2 protective atmosphere (H_2O<1ppm, O_2<1ppm) for 5 days.

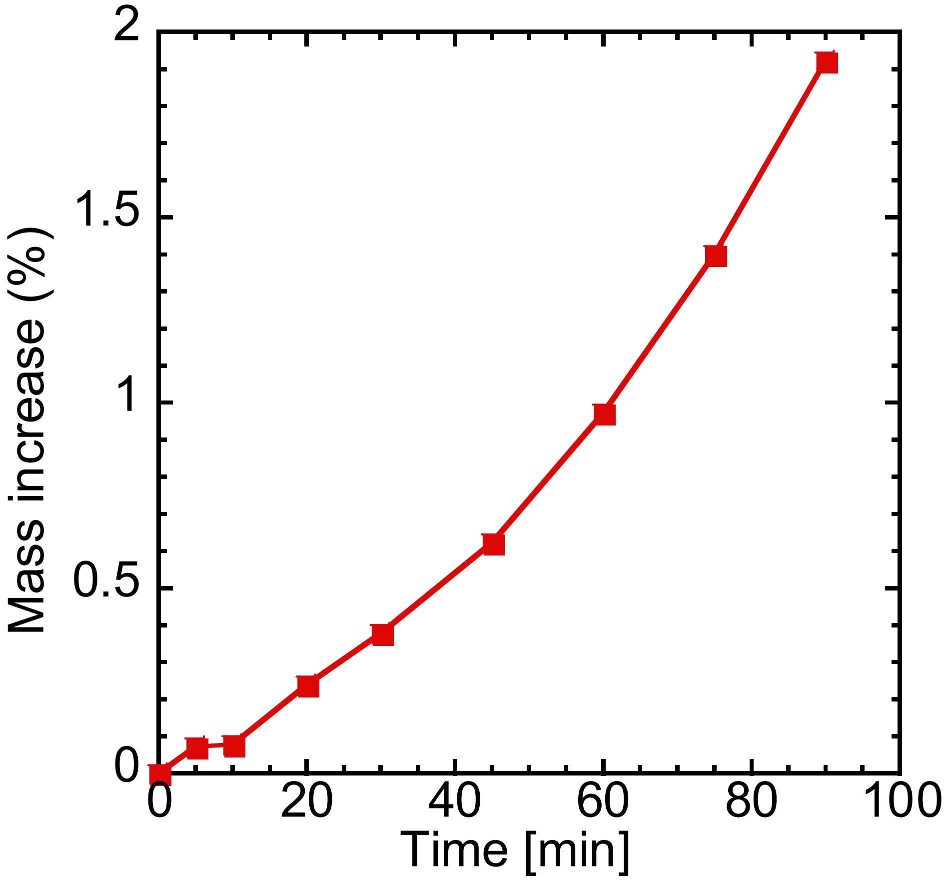

Figure S3. Mass increase in time of the freshly pre-heated La_2O_3 powder up to 1200 °C under N_2 atmosphere left in air under laboratory conditions (25 °C, ca. 25 % relative humidity)

2. Powder preparation

To better understand the phenomena in the studied crystals which originated from the other phases created during the crystal growth, the powder samples of the considered phases were prepared by a solid state reaction and a sol-gel co-precipitation.

2.1. Solid state reaction

The pellets with 6 mm diameter (sample composition: $LaAl_{11}O_{18}$, $La_{0.999}Ce_{0.001}Al_{11}O_{18}$, $La_{0.99}Ce_{0.01}Al_{11}O_{18}$ and $La_{0.80}Ce_{0.20}Al_{11}O_{18}$) were prepared from powders by pressing under the pressure of 1100 MPa. The pellets were annealed in a tube furnace Carbolite HTRH 100-600/18 with a Haldenwanger Alsint 99.7 tube (Type C 799 according to DIN EN 60672) under the flow of 95% argon (6N purity) + 5% H_2 (6N purity) at 1450°C / 20 h. The tube was evacuated by a Pfeiffer HIPACE 80 turbopump at 300 °C until vacuum level 0.001 Pa before entering Ar + 5% H_2 atmosphere into the tube.

The powders for the preparation of the pellets were prepared by a solid state reaction process consisting of several periods of annealing and remixing. The last annealing step for the powders took place in a chamber furnace CLASIC 0518S at 1650 °C / 100 h in air. The powders were laid on sigle-crystalline sapphire boats (manufactured by Crytur from 5N Al_2O_3). The starting materials for the powders preparation were 5N La_2O_3 (Aldrich), 4N7 γ-Al_2O_3 (2.5 Micron Powder Alfa Aesar) and 4N CeO_2 (14 Micron Powder Alfa Aesar). The starting oxides were dried in air at 1200°C / 12 h and the mass losses were 3.89 % w/w for La_2O_3, 9.32 % w/w for γ-Al_2O_3 and 0.35 % w/w for CeO_2. The starting oxides for the powders preparation were weighed with corrections on these losses. The correctness of these corrections was confirmed by the weighing of powders after the sintering steps. Final weight losses were below 0.5 % w/w for all powders.

2.2. X-ray analysis of the powder samples prepared by solid-state reaction

The X-ray diffraction (XRD) of the samples both in the powder and pressed powder pellet forms was measured using RigakuMiniFlex 600 (Ni-filtered Cu-$K_{\alpha 1,2}$ radiation) equipped with the NaI:Tl scintillation detector. The angular range was 10° – 80°, with a step of 0.02° and a scanning speed of 1°/min. The XRD patterns were compared to the relevant records in the ICDD PDF-2 database (version 2013). The lanthanum hexaaluminate (LHA) powder samples were successfully prepared by the solid state reaction avoiding formation of any LaAP phase. The XRD analysis has shown that the samples prepared with the LHA stoichiometry ($LaAl_{11}O_{18}$) contained mostly some other kind of a magnetoplumbite (MP) phase described by the chemical formula $La_{0.827}Al_{11.9}O_{19.09}$ corresponding to the JCPDS 01-077-0311 database pattern. Some samples contained minor impurity phase of metastable LHA superstructure $La_2Al_{22}O_{36}$ (JCPDS 00-028-0502). See figures S4-S6.

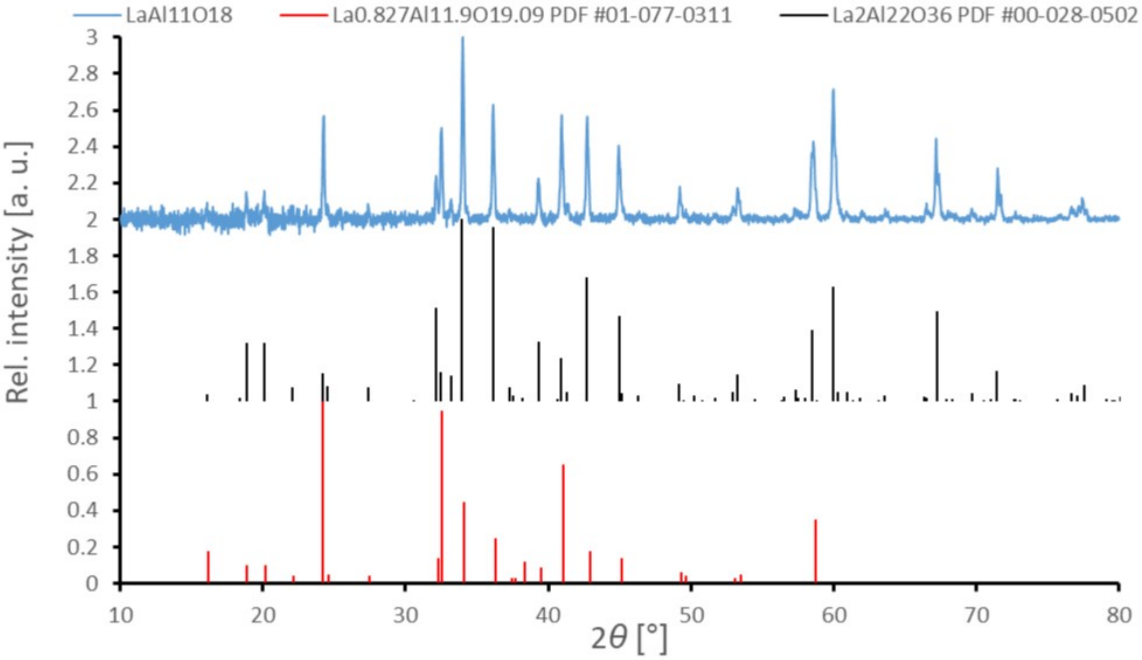

Figure S4. XRD of the undoped $LaAl_{11}O_{18}$ prepared by solid state reaction

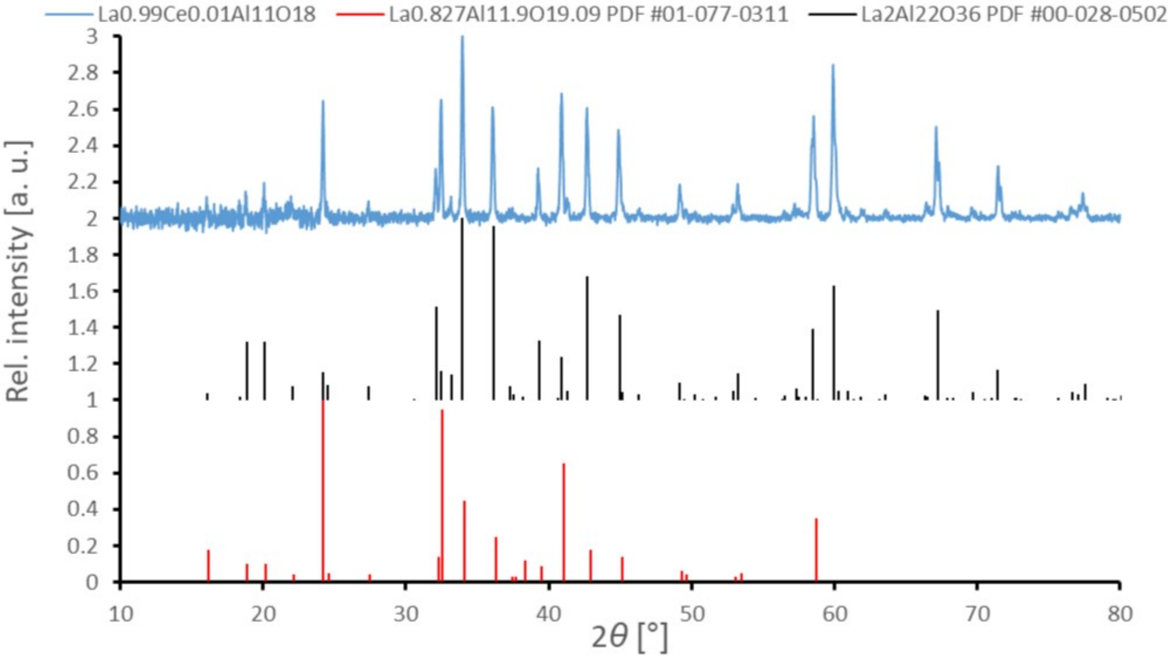

Figure S5. XRD of the $La_{0.99}Ce_{0.01}Al_{11}O_{18}$ prepared by solid state reaction

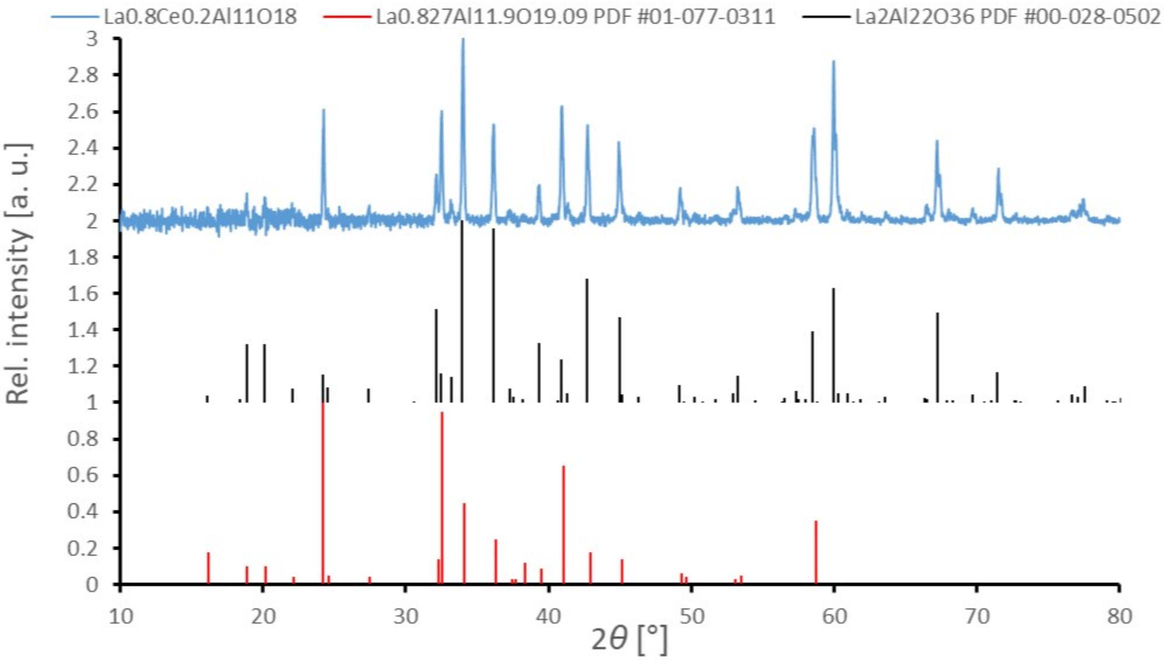

Figure S6. XRD of the $La_{0.8}Ce_{0.2}Al_{11}O_{18}$ prepared by solid state reaction

2.3. Preparation of ceramics samples by a sol-gel method and co-precipitation

Samples with a composition of $(Ce_xLa_{1-x})_{0.86}Al_{11.9}O_{19.14}$ (x = 0-1) were prepared by the Pechini sol-gel process combined with the cold isostatic pressing (CIP). First, anhydrous La(III) and Ce(III) acetates (both 99.9 % REO; Strem Chemicals, inc.) were added to a solution of Al(III) nitrate (Emsure p.a.; Supelco) in a stoichiometric ratio. Then, citric acid (CA; p.a.; Lach:ner) and ethyleneglycol (EG; p.a.; Lach:ner) were added in a “metals:CA:EG” ratio equal to 1:4:16. The solutions was stirred and heated at 80 °C to evaporate water. Finally, the heating temperature was increased to 130 °C to promote the esterification process. The obtained gels were heated at 250 °C/2 h, 600 °C/2 h, and 900 °C/2 h with an intermediate grinding in an agate mortar. The powder precursors were isostatically pressed at 100 MPa and twice annealed in the reducing 5%H_2/95%Ar atmosphere at 1500 °C for 4 hours with the intermediate grinding and re-pressing.

The samples with a stoichiometry of $Ce_xLa_{1-x}AlO_3$ (x = 0.001 and 0.01) were prepared by a reverse co-precipitation method and subsequent annealing. Lanthanum oxide (99.99 % REO; Strem Chemicals, inc.) dissolved in nitric acid 1:1 (p.a.; Lach:ner), cerium acetate (99.9 % REO; Strem Chemicals, inc.) and aluminium nitrate (pure; Lach:ner) were used as the starting compounds in a stoichiometric ratio. The prepared solution was diluted to overall metals concentration of 0.16 mol/l. Next, a precipitation agent solution was prepared by dissolving ammonium hydrogencarbonate (p.a.; Penta) in distilled water with a concentration of 1 mol/L.

The solution of the metals was slowly dropped into the precipitation agent solution with continuous stirring. The volume ratio of the used solutions was 1:1. The obtained suspension was filtered using suction filtration. The filtration cake was rinsed with distilled water and ethanol.

The filtration cake was dried at 120 °C and then annealed at 1000 °C for 1 hour in the air atmosphere. The acquired powder was uniaxially pressed into pellets. The final samples were prepared by annealing of the pellets in the reducing 5%H_2+95%Ar atmosphere at 1200 °C for 2 hours.

2.4. Analysis of the powder samples prepared by a sol-gel method and co-precipitation

The phase composition of the ceramics samples was analyzed using X-ray diffraction (See figure S7). The data were collected at room temperature with a Bruker AXS D2 Phaser powder diffractometer with parafocusing Bragg-Brentano geometry using CoK_{α} radiation (30 kV, 10 mA). The results were processed with the HighScore Plus software (PANanalytical, database PDF-4).

The final samples of the $(Ce_xLa_{1-}x)_{0.86}Al_{11.9}O_{19.14}$ (x=0-1) series contained an Al_2O_3 secondary phase in a concentration range of 5-14 % depending on the Ce/La ratio. The co-precipitated $Ce_xLa_{1-x}AlO_3$ (x=0.001 and 0.01) samples were both single-phase with the rhombohedral crystal structure.

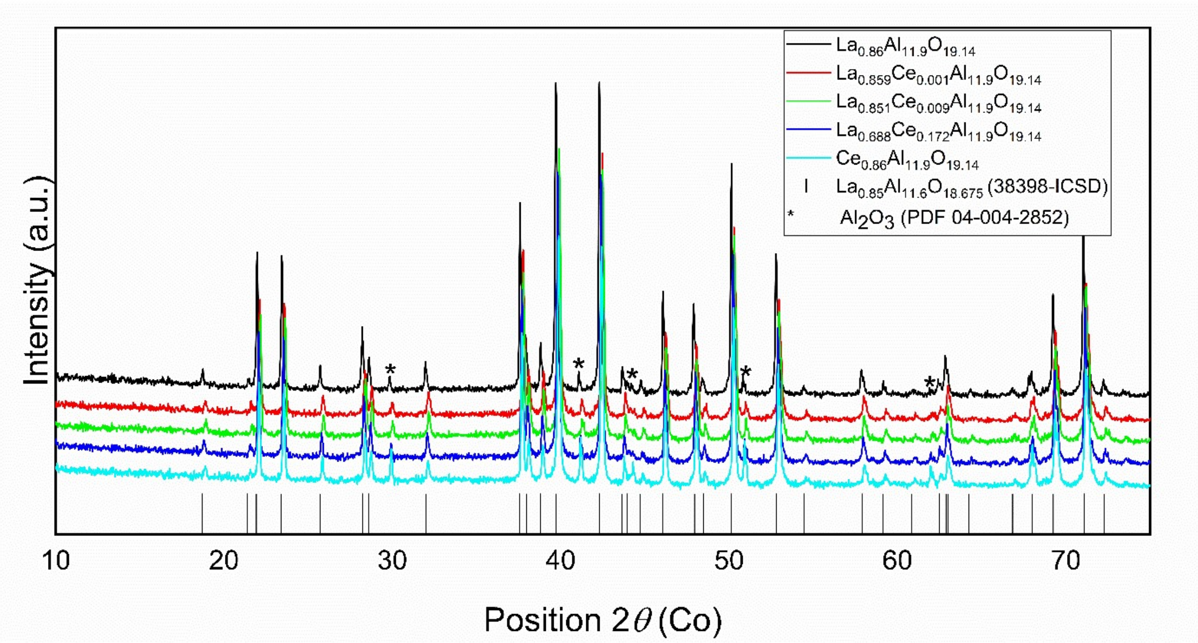

Figure S7. XRD of the $La_{0.86}Al_{11.9}O_{19.14}$ –based powder samples prepared by Pechhini sol-gel process

3. Estimate of the Ce^{3+} emission in LaAP

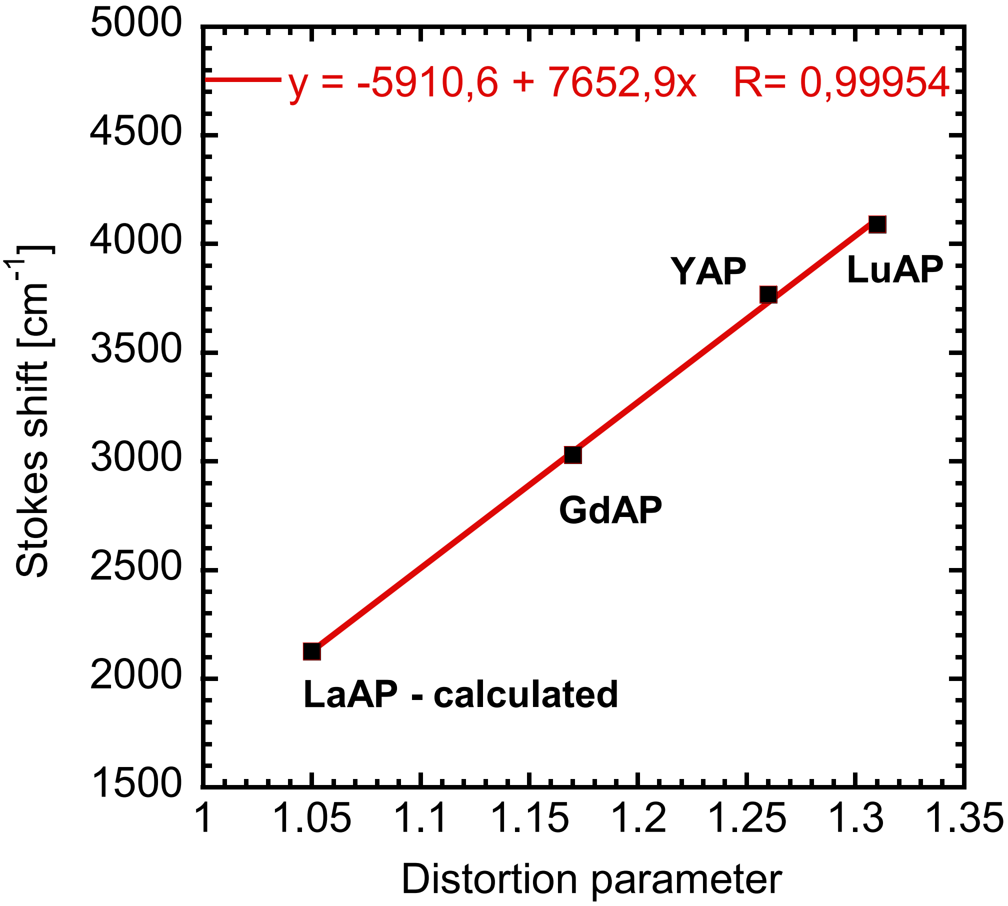

Figure S8. Dependence of the Stokes shift of the Ce^{3+} 5d-4f emission on the cuboctahedron distortion for different perovskites with the fitted linear dependence and extrapolated value for LaAP.

The spectroscopic redshift of the Ce^{3+} 4f-5d transition is determined by the centroid shift and the crystal field splitting, where the former is supposed to be independent of the crystal field strength. All the data for the LaAP and its GdAP ($GdAlO_3$), YAP and LuAP counterparts including the excitation and emission wavelengths, the redshift, the centroid shifts and the crystal field splitting parameters are tabulated in [5]. However, the emission position is determined by the energy of the 4f-5d transition and the Stokes shift, which is unknown for Ce^{3+} emission in LaAP. On the other hand, it is well known for the YAP, GdAP and LuAP counterparts [51]. The Stokes shift is gradually decreasing with increase of the size of the cation residing at the large twelvefold-coordinated cuboctahedral site in the series LuAP → YAP → GdAP. It is therefore expected that the Stokes shift value would be the smallest for LaAP. It is reasonable to ascribe this behavior to the decrease of the twelvefold-coordinated cation radius and the resulting increase of the cuboctahedron distortion, which has a determining influence of the Ce^{3+} luminescence spectroscopy, as shown in [6, 7]. The measure of the distortion can be quantified by the dimensionless distortion parameter defined in [8], where also its values for the above considered perovskite series are reported. The dependence of the Stokes shift on the distortion parameter is plotted in the figure S8. The values for the LuAP → YAP → GdAP series show quite good linear dependence and since the distortion parameter for LaAP is known from the crystal structure data [8], we can extrapolate this dependence towards LaAP and determine the hypothetical Stokes shift to be as small as 2125 cm^{-1}. Considering the lowest Ce^{3+} 4f-5d absorption in LaAP at 317 nm (figure 1 in the article, [9, 10]), the estimated Ce^{3+} emission wavelength would appear around 340 nm. This is quite far from the 370 nm peak observed in the figure 3a in the article, therefore the 370 nm emission is most probably not related to a Ce^{3+} ion situated at the cuboctahedral La site in LaAP, but in a different environment.

4. Photoluminescence decay kinetics of the 30-H2-BS sample

A better insight into the luminescence processes in the 30-H2-BS sample (LaAP:Ce 30%) can be made from the luminescence decay kinetics. The selected results are compared in the figure S9.

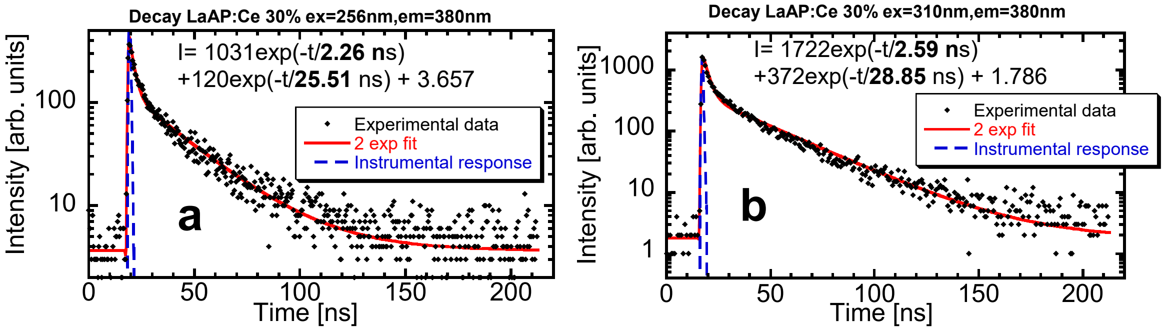

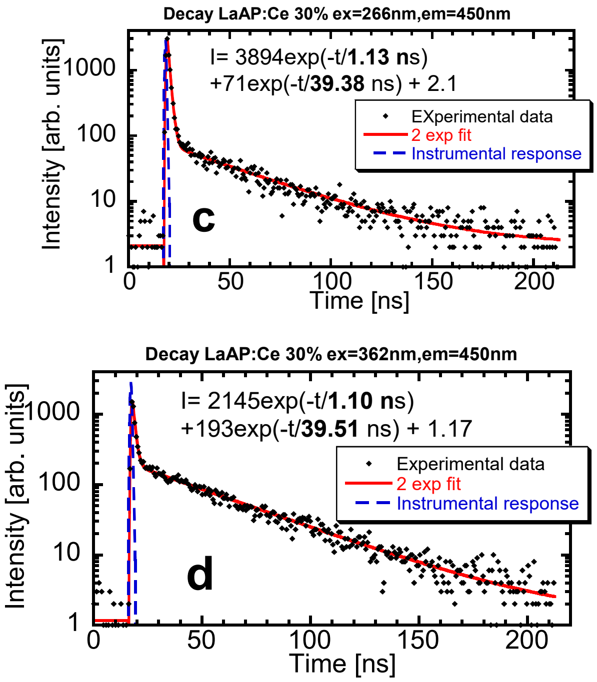

Figure S9. Decay kinetics for 30-H2-BS sample (LaAP:Ce 30%): excitation at 256 nm and emission at 380 nm (a), excitation at 310 nm and emission at 380 nm (b), excitation at 266 nm and emission at 450 nm (c) and excitation at 362 nm and emission at 450 nm (d).

The figures S9a, b show the decay kinetics of the 380 nm emission under 256 and 310 nm excitations. Both decay curves are composed of a fast component with a decay time 2.3-2.6 ns, which can be tentatively ascribed to some defects related to an F^+ center. The emission of such a center in YAP was found around 355 nm with the decay time of 2.7 ns [11], so such an ascription is reasonable. Moreover, since the samples were grown in the reducing atmosphere, creation of oxygen vacancies and related defects is expected. There is a question if this center is related to the LaAP matrix or to an Al-rich inclusion itself. In both decay curves we can observe another component with a decay time of 26 and 29 ns, respectively. Taking into account the discussion in the article and the considerations in [12], it is almost certainly related to the 5d-4f emission of Ce^{3+} residing at the regular La^{3+} site of the magnetoplumbite structure. It is also interesting to compare these results with the decay curve in the figure 3b in the article for the 1-H2 sample, which is characterized with very similar decay time values. The same decay time value for the Ce^{3+} 5d-4f luminescence would either mean that its timing characteristics are independent of the Ce concentration (and therefore no concentration quenching occurs) or the Ce concentration in the inclusions is independent of the sample doping level due to some segregation process. However, the latter statement would contradict the above discussion about the mutual intensities of the Ce^{3+}- and Ce-O associates- related bands. The situation is probably more complicated and needs further research. The figures S9c, d show the decay kinetics of the blue emission at 450 nm. The curves contain a very fast component again probably related to some F^+ center and another longer one with the decay time of almost 40 ns. Such a value is expected for the Ce^{3+} ion at the site with oxygen replacing the large cation nearby, i. e. the emission of the Ce-O associates. As discussed in [8], this site is distorted in a way which increases the emission red shift. This leads to prolongation of the luminescence decay time, which in the case of 5d-4f transition is proportional to the third power of the wavelength [13]. The values observed here match this rule quite well.

5. Emission spectra excited by synchrotron radiation

To get a deeper insight into the luminescence processes and the energy transfer in the studied material, the samples were investigated under synchrotron radiation.

The emission and excitation spectra were measured at room temperature at the MAX IV synchrotron facility in Lund, Sweden, at the FinEstLumi station [14, 15] mounted at the FinEstBeAMS undulator beamline at the 1.5 GeV storage ring of MAX IV [16, 17]. The excitation energy range was 4.5–800 eV. The excitation spectra were normalized utilizing the calibration curve obtained by AXUV-100G diode. The luminescence detection in the UV–visible spectral range (200–800 nm) was performed by the Andor Shamrock (SR-303i) 0.3 m spectrometer equipped with the photomultiplier photon counting heads (H8259-01 Hamamatsu) covering the spectral range from 200 to 900 nm.

The figure S10a shows the emission spectrum of the 1-H2 sample under the 45 eV excitation recalculated to the electronvolt (eV) scale and fitted with three Gaussian curves marked with corresponding peak wavelengths. (The original spectrum in the nanometer scale can be found in the figure S12). It contains a broad band peaking around 3 eV (420-440) nm and is most probably related to the Ce^{3+} emission in the Al-rich inclusions. Despite the lower resolution of the apparatus and less pronounced short-wavelength emission with respect to the photoluminescence (PL) spectra in the article, the Gaussian decomposition shows three distinct bands peaking at 3.33 eV (372 nm), 2.98 eV (416 nm) and 2.58 eV (480 nm). The 372 and 416 nm wavelengths match the values observed in the PL and can be ascribed to the Ce^{3+} at the regular La site in the Al-rich phase and the Ce-O associates, respectively. The difference in their mutual intensities can be caused by a different way of excitation and more significant contribution of the surface states. The 480 nm peak could not be reliably ascribed to any luminescence phenomenon, but might be related to some defect luminescence in the Al-rich phase, as was mentioned in the article. The excitation spectrum in the ultra-violet (UV) and vacuum ultra-violet (VUV) range for the 440 nm emission in the figure S10b is composed of a weak band at 250 nm which is similar to that already observed in the figure 6b in the article and ascribed to the excitation band of the Ce-O associates. It is accompanied by a more intense band peaking around 190 nm. Its long-wavelength onset around 220 nm corresponds well to the onset of the fundamental absorption in the spectrum for the undoped sample in the figure 5 in [1] and also to the value of the energy of the LaAP forbidden gap reported in the literature [18]. The excitation band extends further towards about 168 nm and its width would roughly correspond to the increased density of states at the bottom of the LaAP conduction band consisting mostly of the La^{3+} 5d levels [18, 19, 20]. However, the respective emission apparently originates in the inclusions. Considering the high excitation energy used in the measurement in the figure S10a, it is clear that the collected emission light comes from the surface states, most probably those related to the inclusions. Since the shape of the excitation spectrum resembles to that expected for the LaAP host, there might be an energy transfer to the inclusions from the LaAP matrix. To completely confirm this idea, it would be necessary to know the band structure of the Al-rich phases discussed above. To our best knowledge those are still unknown. However, due to the large amount of Al in the respective compounds, one would expect the band-gap value much larger than that of LaAP, therefore, an energy transfer from the LaAP matrix to the Al-rich inclusions might be impossible or at least difficult. It might be that the 4f-5d transitions of the Ce-O associates lie around similar energies as the band-to-band transitions of LaAP, which, in combination with lower spectral resolution of the synchrotron apparatus would give the broad band at a similar energy. This needs to be verified by further studies.

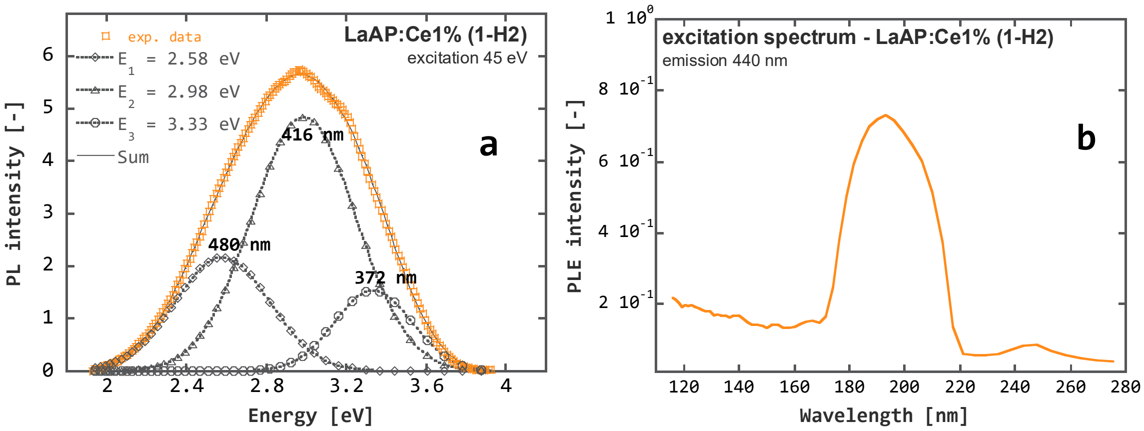

Figure S10. Emission spectrum of the LaAP:Ce1% (1-H2) sample under 45eV irradiation (a) and excitation spectrum of the emission at 440 nm for the same sample (b).

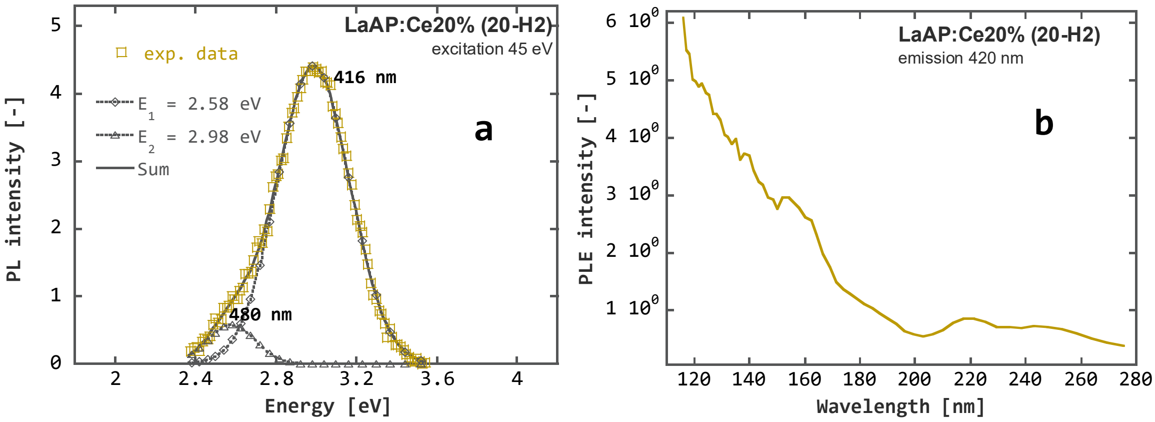

Figure S11. Emission spectrum of the LaAP:Ce20% (20-H2) sample under 45 eV irradiation (a) and excitation spectrum for the emission at 420 nm for the same sample (b)

To observe the influence of an increased Ce concentration, the luminescence spectrum for the 20-H2 sample under 45 eV excitation is shown in the figure S11a (the original spectrum in the nanometer scale is in the figure S13). It contains again the broad band around 3 eV (420-440 nm) related to the Al-rich inclusions, whose shape is a bit narrower than that for the 1-H2 sample (figure S10a). However, now it seems the short wavelength shoulder 380 nm is much less pronounced, what can be expected for the luminescence of inclusions with an increased Ce concentration. The excitation spectrum for the 420 nm emission in the UV-VUV range is shown in the figure S11b. The onset at 220 nm corresponding to the LaAP band-to-band absorption is followed with a dip at 200 nm and then the spectrum rises towards the shorter wavelengths. These are substantial differences when compared to the excitation spectrum of the inclusion luminescence for the 1-H2 sample. It seems that the high Ce^{3+} concentration might modify the conduction band of the host, especially the region consisting of the La^{3+} 5d states.

Interestingly, for some reason the Cr^{3+} impurity luminescence around 720 nm and the other band around 580 nm earlier ascribed to Ce^{3+}-terminated Cr^{3+} emission are now more pronounced (figure S13), which points to the competition between the luminescent centers in the processes of the energy transfer after the high energy excitation well above the band gap.

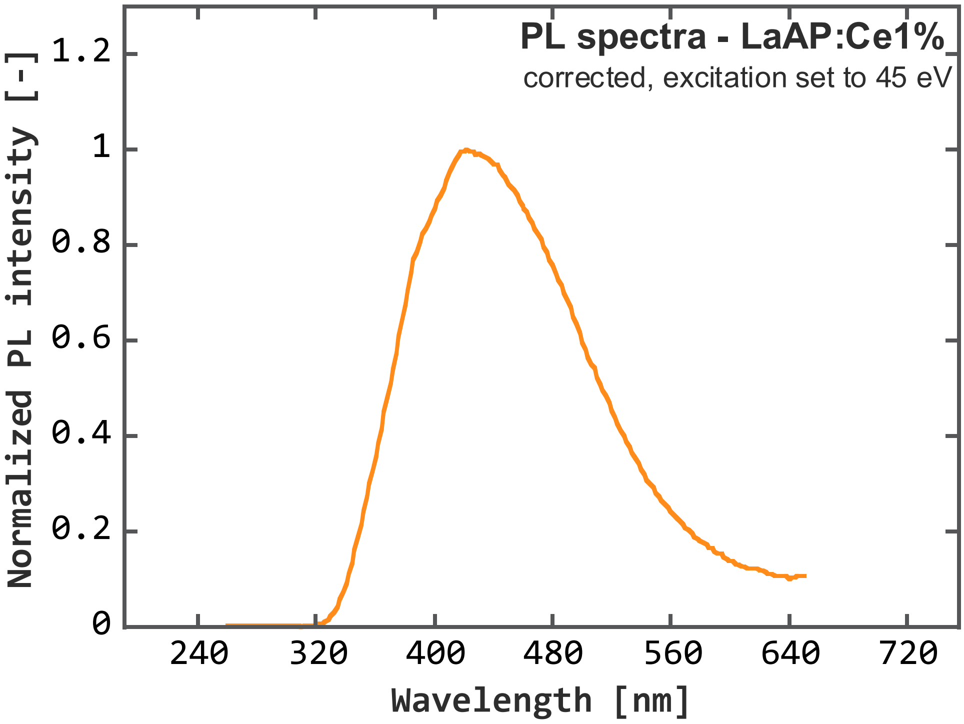

Figure S12. Emission spectrum of the LaAP:Ce1% (1-H2) sample under 45eV irradiation

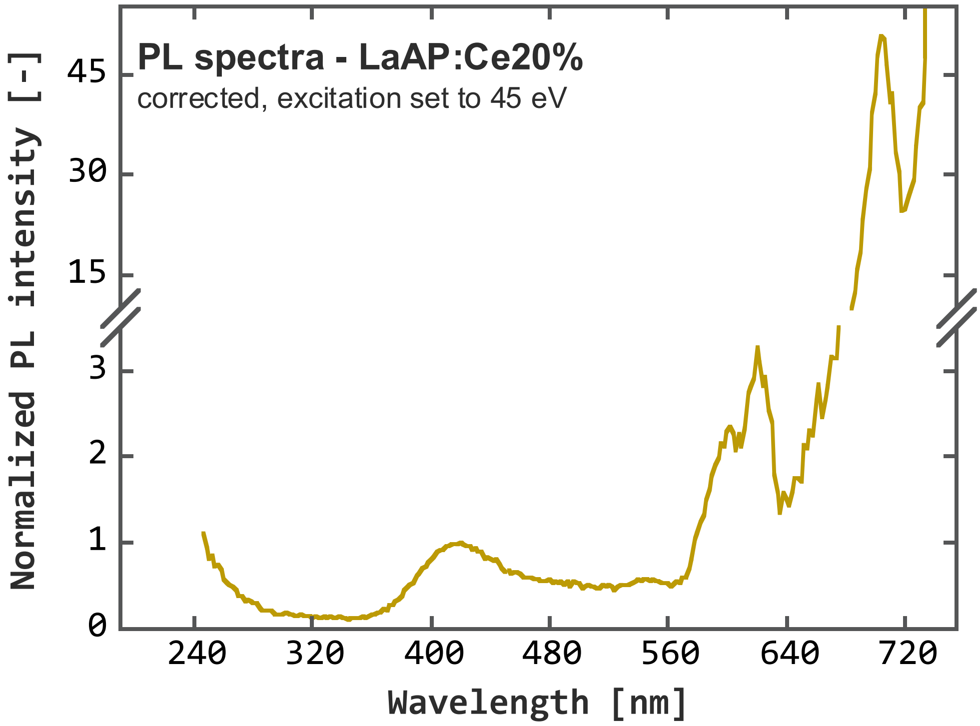

Figure S13. Emission spectrum of the LaAP:Ce20% (20-H2) sample under 45 eV irradiation

6. Luminescence kinetics of the Al-rich powders

The PL decay kinetics for the short wavelength emission at 345 nm for the LHA powder with 20%Ce is shown in the figure S14a. It is single-exponential with a decay time of around 20 ns, which is not so far from the values in the figures S9a,b for the 30-H2-BS sample and can be ascribed to the 5d-4f emission of Ce^{3+} residing at the La site. More complicated decay course for the inclusions in the figures S9a,b might again point to the fact that their composition is not that simple. The decay kinetics of the 440 nm long wavelength band of the same LHA 20%Ce sample is in the figure S14b. It is governed by a single exponential function with a decay time close to 40 ns, which again resembles the values of the decay kinetics for the Ce-O associates in the inclusions shown in the figures S9c,d for the 30-H2-BS sample. The similarities of the luminescence characteristics of the powders with the LHA stoichiometry with the luminescence of the MP powders reported in [12] might be also given by the natural tendency of the LHA to change the stoichiometry and switch to a MP phase as was shown in [21]. This was confirmed also by our XRD analysis that revealed prevailing MP phase with the chemical formula of $La_{0.827}Al_{11.9}O_{19.09}$.

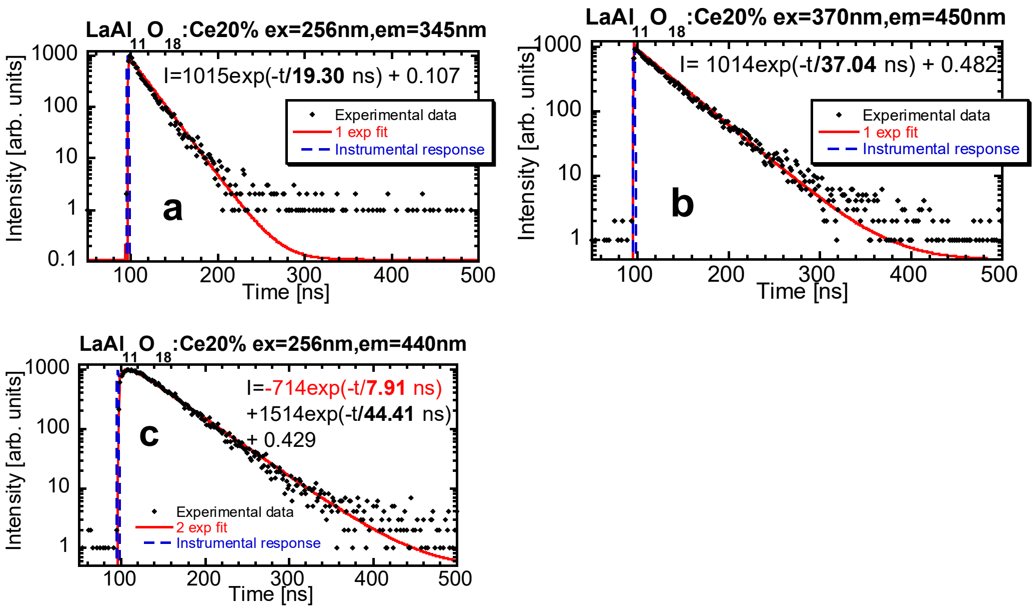

Figure S14. Photoluminescence decay for the undoped $LaAl_{11}O_{18}$ sample for the short wavelength 345 nm emission (a) and long wavelength 440 nm emission under respective excitations (b). The decay time of the 440 nm emission excited under 256 nm wavelength is shown in (c).

Figure S14c shows the decay kinetics of the 440 nm emission under 256 nm excitation, which corresponds to the excitation of the Ce^{3+} at the regular La site in the matrix. It is possible to observe a clear rise at the curve characterized by a rise-time of around 8 ns. This is an apparent sign of an energy transfer. This behavior was described in [12] and was explained by an energy transfer from the Ce^{3+} at La site towards the Ce-O associates. Conversely, this phenomenon was not confirmed in our samples since the rising edge of the decay curves, if it is present, seems to be obscured by some fast luminescence phenomenon, as can be observed for example in the figures S9c,d.

7. Radioluminescence of the LaAP:Ce powders

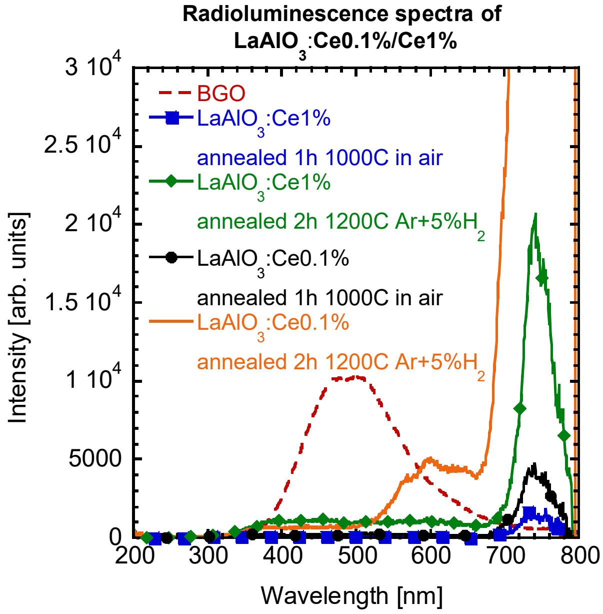

Figure S15. Radioluminescence spectra of the LaAP:Ce powders annealed under various atmospheres compared to the BGO. See the legend for the annealing conditions.

The radioluminescence spectra of the LaAP:Ce powders with 0.1% and 1% Ce annealed in air and under Ar+5%H_2 reducing atmosphere are compared in the figure S15 together with the BGO standard scintillator powder. The Cr^{3+} impurity emission around 740 nm is dominant in all the spectra and it is especially intense for the sample with the low Ce concentration annealed under Ar+5% H_2. The reducing atmosphere seems to have positive influence on the intensity of all the kinds of the observed luminescence. Further research is needed to clarify their origin.

8. Additional electron paramagnetic resonance studies

The electron paramagnetic resonance spectra for the undoped crystalline sample measured at 77 K after an X-ray irradiation are shown for two different orientations of the sample in figure S16a and figure S16b, respectively (the orientation were not indicated in figure S16a,b since the sample was not oriented and cut within the specific crystallographic directions). The signal, almost independent of the sample rotation, referred to an O^- defect was observed at the g factor $g = 2.02$, typical for such kind of a hole trapping center generally in oxides [22-26].

The single resonance line corresponding to the electron spin $S = 1/2$ was ascribed to the high spin state Ir^{4+}. It exhibits an angular dependence in the arbitrary rotation plane if we compare the spectra in figure S16a (overlapped with the O$^-$) and figure S16b. Its *g* factor value measured in the actual arbitrary rotation plane appears in the range 2-2.16. The signal is broad (figure S16b), having a linewidth of about 50 G, so the hyperfine structure of the ^{191,193}Ir (approx. 37 and 63% abundance, respectively, both having nuclear spin $I = 3/2$) nuclei is, most probably, “blurred”. The crystal was grown in the iridium crucible and, therefore, Ir could enter the ingot, for example, as Ir^{3+} during the process of the crystal growth. Being the transition ion it can change its charge state easily under the irradiation or the thermal treatment.

There is also another, very broad signal (linewidth is about 500 G) originating from an unknown trapping center (TC in figure S16a). It is situated at the *g* factor $g \sim 2.4$. It was impossible to determine its origin.

There was also alarge amount of signals tentatively attributed to two centers of Fe^{3+}, an impurity commonly known (typical) and expected in aluminum oxide, aluminum perovskites or garnets, which behave similarly with annealing at the chosen temperatures following the X-ray irradiation. Note, that the spectra in the annealed sample were measured each time at the same constant temperature of 77 K no matter how high was the annealing temperature (T$_{ann}$). For example, the Fe^{3+} resonances in YAP or YAG were described in detail, e.g., in [27, 28].

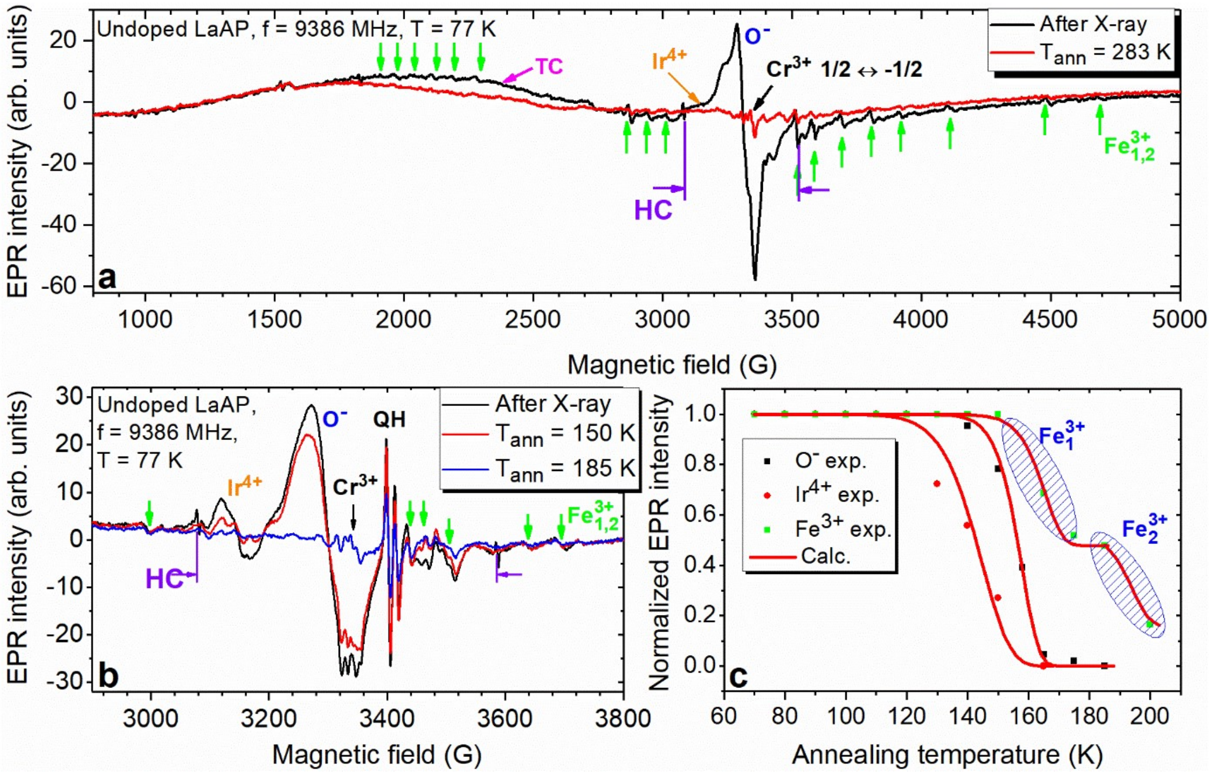

Figure S16. EPR spectra measured in undoped LaAP at 77 K after X-ray irradiation at liquid nitrogen temperature: wide magnetic field range (a) and short magnetic field range (b). The lines originating from Cr^{3+}, $Fe_{1,2}{}^{3+}$, Ir^{4+}, unknown charge trapping center (TC) and hydrogen-related center (HC), and O^- are stressed. "QH" emphasizes a signal from quartz sample holder. c – dependences of the $Fe_{1,2}{}^{3+}$, Ir^{4+} and O^- EPR intensities on annealing temperature (dots represent experimental data whereas solid lines are the fitting curves).

The experimental dependences of the O^-, Ir^{4+} and Fe^{3+} EPR signals on the annealing temperature are shown in figure S16c along with the fitting curves calculated using the following expression for the first order trapping kinetics [29]:

$$I_{i+1} = I_i \exp\left(-f_0 t \exp\left(-E_t \middle/ k_B T_i\right)\right) \tag{1}$$

where I_i, k_B, E_t and f_0 are the EPR intensity in the i-th cycle of the annealing at the annealing temperature T_i for t = 4 minutes, Boltzmann constant, the trap depth and the frequency factor, respectively. The decay of the O^- and Ir^{4+} signals demonstrated monotonous character whereas that of the Fe^{3+} exhibited two steps indicated in Fig. 16c as $Fe_{1,2}^{3+}$, respectively. The following kinetic parameters were determined (Eq. 1): $E_t\left(O^-\right) = 0.40 \pm 0.02$ and $f_0\left(O^-\right)$ ~10^{10} s^{-1}; $E_t\left(Ir^{4+}\right) = 0.20 \pm 0.02$ and $f_0\left(Ir^{4+}\right)$ ~10^4 s^{-1}; $E_t\left(Fe_1^{3+}\right) = 0.42 \pm 0.02$ and $f_0\left(Fe_1^{3+}\right)$ ~10^{10} s^{-1}; $E_t\left(Fe_2^{3+}\right) = 0.57 \pm 0.02$ and $f_0\left(Fe_2^{3+}\right)$ ~10^{12} s^{-1}. As one can see the trap depths and the frequency factors of the $Fe_{1,2}{}^{3+}$ are different. The $E_t\left(Fe_1^{3+}\right)$ and $f_0\left(Fe_1^{3+}\right)$ are approximately the same as those of the O^- center. Therefore, one may conclude that probably in this case the electron trapped at Fe^{3+} recombines with the holes released from the O^- defect. The Fe_2^{3+} is then the result of a thermal destruction of the electron trapped at Fe^{3+}. Based on this one may infer that the iron is present initially as Fe^{4+} in the LaAP sample.

Besides, there was some other doublet of resonance lines indicated as HC (hydrogen-related center) on surface. The splitting within the doublet is 510 G. This kind of resonances is related to the -OH group attached to the surface and was also observed in SiO_2 or Cs_2HfCl_6 after the UV or X-ray irradiation [30-32].

Prior to the X-ray irradiation only the typical resonances of Cr^{3+} were detected which is in a good agreement with the photoluminescence study in the article (subsection 3.2.). The corresponding 1/2 ↔ -1/2 resonances are indicated in figure S16 a,b. There are many resonance lines because of the domain structure of the LaAP. The 3/2 ↔ 1/2 and -3/2 ↔ -1/2 resonances are strongly overlapped with the rest of resonances in figure S16 a,b at this orientation of the crystal with respect to the external magnetic field and thus cannot be resolved. Chromium does not participate in the charge trapping processes at the given conditions.

References

1. J. Pejchal, J. Barta, T. Trojek, R. Kucerkova, A. Beitlerova and M. Nikl, *Radiation Measurements*, 2019, **121**, 26.

2. E. Haibel, E. Füglein, A. S. Schulze and D. Walter, *J Therm Anal Calorim*, 2019, **138**, 3571.

3. X. Zhou, E. I. Vovk, Y. Liu, C. Guan and Y. Yang, *Front. Chem.*, 2021, **9**, 694559.

4. M. Zhuravleva, L. Stand, H. Wei, C. Hobbs, L. Boatner, K. Shah, A. Burger, P. Bhattacharya, E. Tupitsyn and C. Melcher, In *2013 IEEE Nuclear Science Symposium and Medical Imaging Conference (2013 NSS/MIC)*, IEEE, Seoul, Korea (South), 2013, pp. 1.

5. P. Dorenbos, *Journal of Luminescence*, 2000, **91**, 155.

6. E. Mihóková, M. Nikl, M. Bacci, M. Dušek and V. Petříček, *Phys. Rev. B*, 2009, **79**, 195130.

7. Z. Song and Q. Liu, *Phys. Chem. Chem. Phys.*, 2019, **21**, 2372.

8. P. Dorenbos, *Journal of Luminescence*, 2002, **99**, 283.

9. X. Zeng, L. Zhang, G. Zhao, J. Xu, Y. Hang, H. Pang, M. Jie, C. Yan and X. He, *Journal of Crystal Growth*, 2004, **271**, 319.

10. E. van der Kolk, J. T. M. de Haas, A. J. J. Bos, C. W. E. van Eijk and P. Dorenbos, *Journal of Applied Physics*, 2007, **101**, 083703.

11. Yu. V. Zorenko, A. S. Voloshinovskiĭ and I. V. Konstankevych, *Opt. Spectrosc.*, 2004, **96**, 532.

12. A. L. N. Stevels, *J. Electrochem. Soc.*, 1978, **125**, 588.

13. P. Dorenbos, M. Marsman, C. W. E. Van Eijk, M. V. Korzhik and B. I. Minkov, *Radiation Effects and Defects in Solids*, 1995, **135**, 325.

14. V. Pankratov and A. Kotlov, *Nuclear Instruments and Methods in Physics Research Section B: Beam Interactions with Materials and Atoms*, 2020, **474**, 35.

15. V. Pankratov, R. Pärna, M. Kirm, V. Nagirnyi, E. Nõmmiste, S. Omelkov, S. Vielhauer, K. Chernenko, L. Reisberg, P. Turunen, A. Kivimäki, E. Kukk, M. Valden and M. Huttula, *Radiation Measurements*, 2019, **121**, 91–98.

16. R. Pärna, R. Sankari, E. Kukk, E. Nõmmiste, M. Valden, M. Lastusaari, K. Kooser, K. Kokko, M. Hirsimäki, S. Urpelainen, P. Turunen, A. Kivimäki, V. Pankratov, L. Reisberg, F. Hennies, H. Tarawneh, R. Nyholm and M. Huttula, *Nuclear Instruments and Methods in*

Physics Research Section A: Accelerators, Spectrometers, Detectors and Associated Equipment, 2017, **859**, 83.

17. K. Chernenko, A. Kivimäki, R. Pärna, W. Wang, R. Sankari, M. Leandersson, H. Tarawneh, V. Pankratov, M. Kook, E. Kukk, L. Reisberg, S. Urpelainen, T. Käämbre, F. Siewert, G. Gwalt, A. Sokolov, S. Lemke, S. Alimov, J. Knedel, O. Kutz, T. Seliger, M. Valden, M. Hirsimäki, M. Kirm and M. Huttula, *J Synchrotron Rad*, 2021, **28**, 1620.

18. P. W. Peacock and J. Robertson, *Journal of Applied Physics*, 2002, **92**, 4712.

19. R. Pentcheva and W. E. Pickett, *Phys. Rev. B*, 2006, **74**, 035112.

20. A. Boudali, B. Amrani, M. Driss khodja, A. Abada and K. Amara, *Computational Materials Science*, 2009, **45**, 1068.

21. J.-G. Park and A. N. Cormack, *Journal of the European Ceramic Society*, 1999, **19**, 2249.

22. V.V. Laguta, M. Buryi, J. Rosa, D. Savchenko, J. Hybler, M. Nikl, S. Zazubovich, T. Kärner, C.R. Stanek and K.J. McClellan, *Phys. Rev. B*, 2014, **90**, 064104.

23. M. Buryi, D.A. Spassky, J. Hybler, V.V. Laguta and M. Nikl, *Opt. Mat.*, 2015, **47**, 244.

24 A. Watterich, L. Kovács, R. Würz, F. Schön, A. Hofstaetter and A. Scharmann, *J. Phys.: Condens. Matter*, 2001, **13**, 1595.

25. S. Lenjer, O.F. Schirmer and H. Hesse, *Phys. Rev. B*, 2002, **66**, 165106.

26. D. Pan, G. Xu, L. Lu, Y. Yong, X. Wang, J. Wan and G. Wang, *Appl. Phys. Lett.*, 2006, **89**, 082510.

27. L. Rimai and T. Kushida, *Physical Review*, 1966, **143**, 160.

28. I. Stefaniuk, C. Rudowicz, P. Gnutek and A. Suchocki, *Appl Magn Reson.*, 2009, **36**, 371.

29. J. Pejchal, M. Buryi, V. Babin, P. Prusa, A. Beitlerova, Jan Barta, L. Havlak, K. Kamada, A. Yoshikawa, V. Laguta and M. Nikl, *Journal of Luminescence*, 2017, **181**, 277.

30. M. Buryi, V. Babin, R. A. M. Ligthart, S. S. Nagorny, V. B. Mikhailik, V. Vaněček, L. Prouzová Prochazková, R. Kandel, V. V. Nahorna and P. Wang, *J. Mater. Chem. C*, 2021, **9**, 2955.

31. A. M. Monti, M. Buryi, M. Fasoli and M. Martini, *Radiation Measurements*, 2021, **145**, 106604.

32. D. L. Griscom, *Nuclear Instruments and Methods in Physics Research Section B: Beam Interactions with Materials and Atoms*, 1984, **1**, 481.